Sensing and Bio-Sensing Research 30 (2020) 100375

Contents lists available at ScienceDirect

Sensing and Bio-Sensing Research

journal homepage: www.elsevier.com/locate/sbsr

Real-time measurement of tumour hypoxia using an implantable microfabricated oxygen sensor

Jamie R.K. Marland[a,*], Mark E. Gray[b], Camelia Dunare[a], Ewen O. Blair[a,1], Andreas Tsiamis[c], Paul Sullivan[a], Eva González-Fernández[d], Stephen N. Greenhalgh[b], Rachael Gregson[b], R. Eddie Clutton[b], Magdalena M. Parys[b], Alex Dyson[e], Mervyn Singer[e], Ian H. Kunkler[f], Mark A. Potter[g], Srinjoy Mitra[a], Jonathan G. Terry[a], Stewart Smith[c], Andrew R. Mount[d], Ian Underwood[a], Anthony J. Walton[a], David J. Argyle[b], Alan F. Murray[c]

[a] School of Engineering, Institute for Integrated Micro and Nano Systems, The University of Edinburgh, Scottish Microelectronics Centre, Edinburgh EH9 3FF, UK
[b] The Royal (Dick) School of Veterinary Studies and Roslin Institute, University of Edinburgh, Easter Bush, Roslin, Midlothian EH25 9RG, UK
[c] School of Engineering, Institute for Bioengineering, The University of Edinburgh, Faraday Building, Edinburgh EH9 3DW, UK
[d] School of Chemistry, University of Edinburgh, Joseph Black Building, Edinburgh EH9 3FJ, UK
[e] Bloomsbury Institute of Intensive Care Medicine, Division of Medicine, University College London, Gower Street, London WC1E 6BT, UK
[f] Cancer Research UK Edinburgh Centre, Institute of Genetics and Molecular Medicine, University of Edinburgh, Crewe Road South, Edinburgh EH4 2XU, UK
[g] Department of Surgery, Western General Hospital, Crewe Road, Edinburgh EH4 2XU, UK

ARTICLE INFO

Keywords:
Oxygen sensor
Tumour hypoxia
Implantable
Microfabrication

ABSTRACT

Hypoxia commonly occurs within tumours and is a major cause of radiotherapy resistance. Clinical outcomes could be improved by locating and selectively increasing the dose delivered to hypoxic regions. Here we describe a miniature implantable sensor for real-time monitoring of tissue oxygenation that could enable this novel treatment approach to be implemented. The sensor uses a solid-state electrochemical cell that was microfabricated at wafer level on a silicon substrate, and includes an integrated reference electrode and electrolyte membrane. It gave a linear response to oxygen concentration, and was unaffected by sterilisation and irradiation, but showed susceptibility to biofouling. Oxygen selectivity was also evaluated against various clinically relevant electroactive compounds. We investigated its robustness and functionality under realistic clinical conditions using a sheep model of lung cancer. The sensor remained functional following CT-guided tumour implantation, and was sufficiently sensitive to track acute changes in oxygenation within tumour tissue.

1. Introduction

Hypoxia commonly occurs within solid tumours due to disorganised growth of blood vessels. It is often spatially heterogeneous and can change with time [1,2]. Unfortunately hypoxia also causes resistance to radiotherapy, with cancer cells in low oxygen environments able to withstand radiation doses 2–3 times higher than aerobic cells [3]. Hypoxia is also associated with malignant progression and poor clinical outcome [4]. Knowledge of the location and degree of hypoxia within a tumour could therefore be used to personalise and improve radiotherapy by matching the dose distribution to treatment sensitivity – a concept known as “dose painting” [5]. This has the potential to improve cancer treatment by optimising its effectiveness while minimising side effects. Advanced techniques for achieving the necessary precise dose delivery such as Intensity Modulated Radiotherapy are already in widespread use [6], but there is no clinically applicable technique for continuous real-time measurement of tumour hypoxia.

Existing medical imaging techniques that can measure tumour hypoxia, such as positron emission tomography (PET) and magnetic resonance imaging, provide only qualitative measurements, have limited spatial resolution, and give only a single time-point, limiting their usefulness [7]. In addition, PET scans result in radiation exposure, limiting the frequency with which they can be safely used. Quantitative imaging of hypoxia using electron paramagnetic resonance imaging is under development, but will require advances in readout technologies and the use of probe compounds that are not currently approved for use in humans [8]. Direct measurement of oxygen within tumours is possible using the Eppendorf polarographic needle electrode. This is a

* Corresponding author.
E-mail address: jamie.marland@ed.ac.uk (J.R.K. Marland).
[1] Present address: Department of Biomedical Engineering, University of Strathclyde, Glasgow, G4 0NS, UK.

https://doi.org/10.1016/j.sbsr.2020.100375
Received 11 June 2020; Accepted 6 August 2020
Available online 11 August 2020

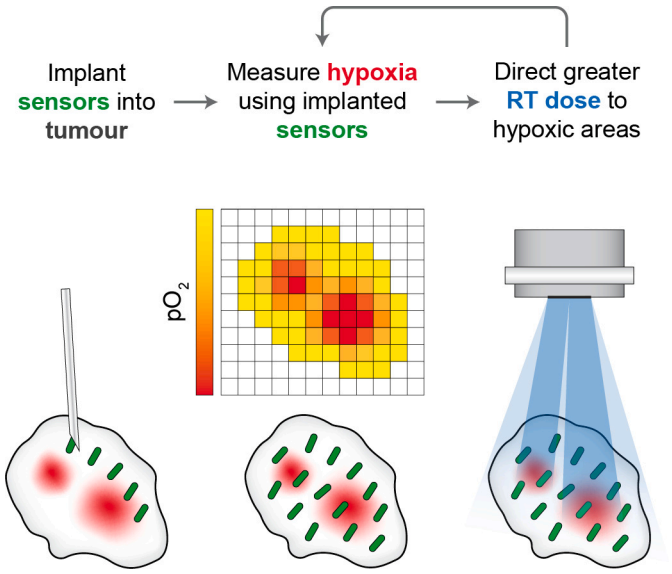

Fig. 1. Personalised radiotherapy treatment concept. Miniature implantable tissue oxygen sensors (green) are implanted into a tumour (grey) containing hypoxic regions (red). Real-time data from an array of implanted sensors is then used to generate a 3D map of hypoxia within the tumour. This map can inform radiotherapy (RT) dose planning and delivery, with a greater dose (blue) being directed to the hypoxic areas that are more resistant to treatment. The measurement process is then repeated using the same sensors prior to each radiotherapy fraction, enabling the treatment to be continuously personalised.

transcutaneous electrochemical sensor that can be mechanically stepped through tissue along a linear track to measure hypoxia. It has been used extensively in research settings [9], but is not clinically applicable as it requires an invasive procedure for each measurement and again only gives single time-point measurements.

To overcome these limitations and deliver continuous real-time sensing for personalised radiotherapy treatment, we have developed and tested a miniature implantable sensor that could be inserted into multiple regions of a tumour. This would enable the construction of a real-time hypoxia map, allowing personalised adaptations to radiotherapy dose distribution during a course of treatment (Fig. 1) [10]. This type of implantable sensor was seen as acceptable by the majority cancer patients we recently surveyed [11].

The sensor is based on electrochemical oxygen detection. This is the simplest method of measuring oxygen concentration and was first described in 1897 by Danneel and Nernst [12]. Following their discovery, a series of innovations culminated in the “Clark electrode” oxygen sensor in 1956, which can reliably operate in biological media [13]. The Clark electrode is an amperometric sensor, detecting oxygen at a platinum electrode via a reduction reaction that produces a current proportional to the oxygen concentration [14]. A key development was separation of its bare electrodes and their liquid electrolyte from external biological media using a gas permeable membrane. This prevents dissolved proteins and metabolites from interfering with the electrode and impairing its ability to sense oxygen [15]. However, conventional Clark electrode sensors are still typically unsuitable for implantation as they are bulky and contain a liquid electrolyte. To overcome these problems, we have developed a miniature Clark-type oxygen sensor that is specifically designed for implantation. Silicon based microfabrication techniques were used throughout the sensor fabrication process, as they allow straightforward miniaturisation, excellent reproducibility, and low manufacturing cost in volume. Crucially, they also open the possibility of future integration with complementary metal-oxide-semiconductor (CMOS) instrumentation electronics.

The miniature sensor is based on a three-electrode cell, with a platinum working electrode (WE) at which oxygen reduction occurs, a Ag/AgCl reference electrode (RE) that provides a fixed electrochemical potential against which the WE potential can be accurately set, and a platinum counter electrode (CE). We selected a Ag/AgCl RE because it is well tested in biosensing applications and is more straightforward to miniaturise than other standard REs [16]. The sensor surface is coated with a thin-film of the porous ionomer Nafion that allows transport of water and protons [17], combining the functions of both an electrolyte matrix and membrane into a single layer. This enables the device to be fully solid-state. Several other designs of microfabricated electrochemical oxygen sensors have previously been described [18–31], highlighting the broad interest in this technology. However, to date no design has been reported that is not only amenable to wafer-level CMOS post-processing, and integrated with a stable on-chip RE and membrane, but also successfully validated in an implantable application. Here we describe the microfabrication and testing of a sensor platform that meets all these criteria, and show proof-of-principle operation within an ovine lung tumour.

2. Material and methods

2.1. Electrode fabrication

Sensors were fabricated on 100 mm diameter, *n*-type, < 100 > orientation silicon wafers (Si-Mat). A bottom insulator layer of 500 nm silicon dioxide was grown by thermal oxidation. Electrodes and interconnect were fabricated from a layer of 50 nm Pt on top of a 10 nm Ti adhesion layer, both deposited by electron beam evaporation, patterned using photolithography, and etched in Ar plasma. A 1000 nm layer of aluminium was sputtered onto the surface and patterned using a lift-off process to form bond pads. The wafer surface was passivated with 500 nm of silicon nitride, followed by 250 nm of silicon dioxide to promote adhesion of the Nafion membrane [32]. Both passivation layers were deposited using high-frequency plasma enhanced chemical vapour deposition. Openings to the electrode and bond pad areas were then defined in the passivation by photolithography and subsequent processing in a CHF_3 / Ar plasma (to etch silicon dioxide) followed by CF_4 / O_2 plasma (to etch silicon nitride). For the RE, early testing showed that bare platinum did not produce a sufficiently consistent potential, so instead we used an additional Ag/AgCl layer on the RE surface to provide a fixed and stable electrochemical potential. A 500 nm layer of silver was deposited by electron beam evaporation and patterned over the RE area using a lift-off process. To chloridise the silver, a protective layer of photoresist was first deposited over the aluminium bond pads to prevent their oxidation, and then the wafer was dipped in 50 mM aqueous $FeCl_3$ for 60 s at room temperature, which deposited a solid layer of AgCl on the RE surface. After chloridisation the protective photoresist was removed by wet stripping.

2.2. Nafion membrane stack fabrication

The Nafion membrane was designed to cover all three electrodes, as it has previously been shown to generally reduce electrode biofouling [33,34] and to extend Ag/AgCl RE lifetime [35]. We found that microfabrication of Nafion structures was challenging, as the layer was easily damaged during wafer processing and packaging. We therefore developed a novel method to deposit and protect it during these steps. The wafer surface was first treated in a solution of 2% Silane A174 (3-(Trimethoxysilyl)propyl methacrylate) in ethanol for 5 min at room temperature to promote Nafion adhesion [23,28], then dried at 60 °C for 30 min. A solution of 5% Nafion in lower aliphatic alcohols and water (274704, Sigma-Aldrich) was then spin coated onto the wafer at 150 rpm for 10 s, followed by 500 rpm for a further 30 s. The layer was air dried at room temperature and annealed at 120 °C for 5 min on a hotplate. SPR350 photoresist (Dow) was deposited by spin coating at 1000 rpm for 60 s, soft-baked at 90 °C for 90 s, patterned using photolithography to define the membrane area, and then developed for

1 min. An MF-26A developer solution (Dow) diluted to 2:1 (developer : water) was used to prevent attack of the Nafion surface [32]. The Nafion was etched in O_2 plasma, and the photoresist was left in place following etching as an over-etch buffer for later steps (Fig. S1a). Finally, to provide solvent resistance, a temporary protective layer of 500 nm Parylene-C was deposited by chemical vapour deposition, patterned using photolithography to cover the Nafion layer, and etched in O_2 plasma (Fig. S1b). Together these layers protected the Nafion from vigorous cleaning processes during packaging. The final membrane was characterised using a DektakXT surface profiler on test dies from which the protective layers had been stripped.

2.3. Sensor packaging

Sensors were diced into 2 mm × 3 mm chips and mounted on the end of a custom six-track flexible PCB (Merlin Flex Ltd) using Loctite 4014 biocompatible adhesive. The flexible PCB had dimensions of 1.7 mm × 200 mm (for bench testing) or 1.7 mm × 500 mm (for sheep implantation). Connections from the sensor bond pads to the flexible PCB were made using gold wire bonds. Bonds were made from each pad to two adjacent tracks on the PCB, allowing verification of the pad connection after implantation by testing electrical continuity between the tracks. The sensor assembly was encapsulated in OG116–31 photocurable biocompatible epoxy (Epoxy Technology, Inc.) that was selectively cured by exposure to ultraviolet (UV) light to form a hermetic package around the die and bonds. The external dimensions were approximately 2.8 mm × 5.1 mm × 1.4 mm (W × L × H), and an unexposed region approximately 1.4 mm × 1.8 mm was left over the sensor active area. The packaging dimensions were designed to be compatible with delivery through an 8G Jamshidi needle. Unexposed epoxy was manually removed from the outside of the package and internal sensor area using acetone. Epoxy was then deposited on the back of the sensor and cured by flood UV exposure. Following encapsulation, the protective Parylene-C layer on the sensor die surface was removed using O_2 plasma etching, and the photoresist layer on the Nafion was removed by dipping in MF-26A developer for 10–15 s, followed by immersion in water (Fig. S1c). Finally, the epoxy encapsulation was heat cured at 80 °C for 2 h to ensure biocompatibility and maximum mechanical strength. The flexible PCB was connected to potentiostat instrumentation through a miniature edge connector (XF3M-0615-1B-R100, Omron).

2.4. Scanning electron microscopy and focused ion beam milling

The RE surface was inspected during fabrication using a Tescan Vega3 XMU scanning electron microscope. Surface composition was characterised using an energy dispersive X-ray spectroscopy detector at 12.5 kV beam energy over a 10 μm × 7.5 μm field. For each sampled area, 1×10^5 counts were analysed using Bruker EDS software. Die cross-sections were milled using a FEI Strata 200XP focussed ion beam system with a 30 kV gallium beam. Milled die samples were coated in a thin layer of evaporated gold to protect the polymer layers prior to imaging.

2.5. Electrochemical characterisation

An Autolab PGSTAT12 bench potentiostat (Metrohm AG), controlled using Nova software, was used for sensor characterisation. For stability and lifetime testing a MUX.MULTI4 multiplexer (Metrohm AG) was also used to allow sequential measurement of the sensor RE potential and WE current. CV measurements were performed using a 2 mV step size and 100 mV/s scan rate. All reagents used for electrochemical characterisation of sensors were obtained from Sigma-Aldrich, and were used as received. Chemical permeability testing of the Nafion membrane was performed in a solution of 1 mM $K_3[Fe(CN)_6]$, 1 mM $K_4[Fe(CN)_6]$, and 100 mM KCl. Sensor performance was measured in phosphate buffered saline (PBS) containing 154 mM NaCl and 10 mM phosphate buffer at pH 7.4. The RE response to changing pH was characterised in PBS at the same constant NaCl concentration, but with different pH values set by adjusting the ratio of monobasic to dibasic sodium phosphate. To characterise the RE response to chloride, aqueous NaCl was varied in concentration between 10 mM and 300 mM, while holding the total ionic strength constant at 300 mM using $NaNO_3$. On-chip RE potentials were measured relative to a commercial Ag|AgCl|KCl (3 M) reference electrode (Sigma-Aldrich). Linearity and sensitivity of the oxygen response were measured at atmospheric pressure in PBS that was bubbled with different mixtures of oxygen and nitrogen. The gas composition was set using a custom gas mixing rig that was manually adjusted to achieve specific dissolved oxygen concentrations, which were directly measured in solution using a Seven2Go S9 meter with an InLab OptiOx probe (Mettler Toledo). Biofouling experiments were performed in air-saturated PBS containing 35 mg/mL BSA, and interference experiments were performed in air-saturated PBS containing either 3 μM hydrogen peroxide, 375 μM uric acid, 45 μM ascorbic acid, or 100 μM paracetamol.

2.6. Sensor sterilisation and irradiation

Sensors were sterilised in ethylene oxide gas produced using an Anprolene AN-73 EtO gas ampoule (Andersen Products) at room temperature and pressure for 12 h, then left to degas for at least 2 h before use. For irradiation testing, sensors were immersed in 1.5 cm of PBS to provide a build-up region, and then exposed to a total radiotherapy dose of 24 Gy, delivered in four fractions of 6 Gy at 3 min intervals, under a 6 MV beam from a Varian Clinac 2100C/D linear accelerator (Varian Medical Systems).

2.7. Lung tumour implantation

Sheep studies were performed under a UK Home Office Project Licence in accordance with the Animals (Scientific Procedures) Act 1986 and approval from the University of Edinburgh Animal Welfare and Ethical Review Boards. Three adult female sheep (Highlander, $n = 1$; Scottish blackface, $n = 2$), weighing 52–65 kg and diagnosed with naturally occurring pre-clinical ovine pulmonary adenocarcinoma, were obtained through an on-farm ultrasound eradication programme [36,37]. Sheep were housed in groups of at least two animals, bedded on straw, with ad libitum access to food and water. Anaesthesia and analgesia were managed by a team of specialist veterinary anaesthetists. The clinical management and surgery of these cases has previously been described [38]. All animals received a central venous cannula placed in the jugular vein which was used for administering drugs and crystalloid fluids. An arterial cannula was also placed in the central auricular artery for monitoring arterial blood pressure and to obtain arterial blood samples. Intermittent blood-gas, biochemical, and haematological analysis was performed with an Epoc portable blood gas electrolyte and critical care analyser (Woodley Equipment Company). Pulse rate and blood pressure along with pulse oximetry, capnography, temperature, spirometry, electrocardiography and inspired and expired gases (O_2, CO_2, and inhalant anaesthetic agent) were continuously monitored using a Datex-Ohmeda S/5 multiparameter patient monitoring device (SOMA Technology). All animals were euthanised with intravenous sodium pentobarbitone (Animalcare). CT imaging procedures were performed using a single-section SOMATOM Definition AS 64 slice helical CT machine (Siemens Healthcare) [38].

All experiments were conducted on anaesthetised, non-recovery animals. Sensors were inserted using a trans-thoracic percutaneous technique under CT guidance using an 8G × 15 cm Jamshidi biopsy needle (Carefusion). An initial CT scan was used to select an OPA lesion and plan the needle path trajectory for sensor implantation. Non-metallic, radiopaque grid lines (GuideLines, Oncology Imaging Systems) placed on the thoracic wall skin surface and intercostal spaces aided

lesion localisation and determined the site for percutaneous sensor placement. Implantation was performed as previously described [38]. Briefly, a small skin incision was made approximately 1–2 intercostal spaces caudal to the desired entry point into the thoracic cavity through which the biopsy needle with its stylet in place was inserted. The needle was advanced cranially through subcutaneous tissues, then pushed through the chest wall at the desired intercostal space. A CT scan confirmed correct needle positioning before it was seated into the OPA tumour. Serial CT scans and needle advancements were made until the needle was positioned centrally within the tumour. Once positioned the stylet was removed, and a sterilised sensor and lead were introduced down the bore of the needle and pushed past the tip of the needle into OPA tissue. The implantation needle was withdrawn, leaving the sensor and lead wire in situ which was then sutured in place. A CT scan was performed to evaluate sensor positioning prior to testing, and a final scan was performed post-mortem to ensure the sensor had remained in place.

To assess the ability of the implanted sensors to detect changes in intratumoral pO_2 through changes in blood oxygenation, a series of alterations in target fraction of inspired oxygen (FiO_2) was performed. The cycle of FiO_2 alterations was: 1.00 (baseline), 0.50 (inducing mild hypoxaemia), 0.21 (inducing moderate hypoxaemia) before finally returning to 1.00. Each FiO_2 step was performed for approximately 20 min (exact timings varied slightly according to clinical need, and are shown in Fig. S5). Arterial blood samples were taken at the end of each step.

2.8. Statistical analysis

Data were tested for normality using the Shapiro-Wilk test. Parametric testing on normally distributed data was performed using two-tailed paired *t*-tests to compare between two groups, and a repeated measures one-way ANOVA followed by Dunnett's post-hoc test to compare between three or more groups. For non-normally distributed data, a two-tailed Wilcoxon matched-pairs signed rank test was used to compare between two groups. Non-linear regression with a semi-log line was used to fit the RE response to chloride concentration, and linear regression was used to fit the RE response to pH and the sensor response to oxygen partial pressure. Fitted parameters were compared to theoretical values using an extra sum-of-squares F-test. Statistical analysis was carried out using Prism 8 (GraphPad). Values in the text and figures are presented as mean ± standard deviation (SD).

3. Results

3.1. Sensor fabrication

Each sensor consists of a three-electrode electrochemical cell containing a 50 μm diameter circular WE, surrounded by a RE and CE with a WE:RE:CE area ratio of 1:3:10. The sensors were microfabricated on a silicon wafer, using conventional thin-film techniques to create platinum electrodes and external aluminium bond pads, followed by production of a Ag/AgCl layer on the RE by chemical oxidation of a thin-film of silver (Fig. 2a,b). Formation of AgCl was monitored using scanning electron microscopy with energy dispersive X-ray spectroscopy (SEM/EDX). X-ray peaks corresponding to silver were readily identified on the RE area prior to chloridisation, and additional elemental chlorine peaks corresponding to chloride were evident following chloridisation (Fig. 2c). Inspection of the surface using SEM showed that the initially smooth evaporated silver surface was modified by chloridisation, with granular structured AgCl growing on and into the electrode surface (Fig. 2d i-iii). The Ag/AgCl layer was also examined in cross-section using focussed ion beam milling followed by SEM. This showed a clearly visible layer of Ag/AgCl over the RE area, although there was no distinct division between the two materials, suggesting either a diffuse interfacial boundary or that little metallic silver remained (Fig. 2d iv). Separate investigation of the chloridisation process using a series of microfabricated silver thickness test structures confirmed that the latter was the case [39]. Since the Ag/AgCl layer was fabricated on an underlying layer of platinum, an electrically conductive path to the RE was maintained despite the highly efficient chloridisation.

The Nafion membrane was then fabricated over the electrodes. To integrate this layer with subsequent wafer processing and packaging, we developed a novel series of processes in which Nafion was spin-coated on the wafer, thermally annealed, patterned using photolithography and plasma etched at wafer level, and then temporarily protected using sacrificial layers of photoresist and Parylene-C (Fig. 2a and Fig. S1a,b). Fabricated sensor dies were wire bonded to a flexible printed circuit board (PCB) lead for connection to external instrumentation, and photocurable epoxy was used to selectively encapsulate the die edges, leaving an uncured window over the sensor active area (Fig. 2e,f) [40]. Finally, the protective layers were removed from the Nafion membrane prior to use (Fig. S1c). The final Nafion layer thickness was 518 ± 32 nm (n = 10 devices, from two wafers), measured by profilometry.

3.2. Sensor characterisation

Performance of the on-chip Ag/AgCl RE in packaged sensors was characterised in PBS against a commercial Ag/AgCl RE with an internal 3 M KCl filling solution. The median on-chip RE potential was +74.0 mV (inter-quartile range: +71.7 to +76.4 mV, n = 81 sensors, from two wafers), confirming that the fabrication process had produced a functional and reproducible RE. We hypothesised that the small positive potential difference was due to the lower chloride activity in PBS contacting the on-chip RE compared to the concentrated KCl filling solution of the commercial RE, rather than a Donnan membrane potential [41]. To confirm this, the concentration of sodium chloride in solution bathing the sensor was varied while holding the ionic strength constant using sodium nitrate to maintain constant activity. The on-chip RE potential changed with the logarithm of chloride concentration, giving a slope of −58.6 mV/dec (Fig. S2a). This was not significantly different to an ideal Nernstian response of −58.2 mV/dec, supporting the hypothesis. The response of the RE to changing pH was also evaluated in PBS over a physiological range of pH 6.2–7.8, and showed no significant variation, as expected (Fig. S2b).

To establish whether the Nafion layer was acting as a protective sensor membrane in the packaged sensors, we performed cyclic voltammetry (CV) at the WE in a solution of potassium ferricyanide and potassium ferrocyanide. The ferri/ferrocyanide anions should be excluded from Nafion (due to their size and/or charge), and thus blocked from reacting at the WE. Consistent with this, no redox processes were visible in the cyclic voltammograms from Nafion coated sensors. In contrast, control devices lacking a Nafion membrane showed clear peaks corresponding to the reduction and oxidation of the ferro/ferricyanide in solution, indicating their presence at the electrode surface (Fig. 3a). These results show that the fabricated Nafion membrane fully covered the WE surface and that no defects were introduced into the layer during packaging. In addition, they confirm that the epoxy packaging was effective at hermetically sealing the bond pads and wire bonds from contact with external solutions.

To characterise the electrochemical performance of the complete sensor system we performed CV in PBS using the on-chip WE, RE and CE. The WE potential was swept between −0.7 V and +0.9 V (vs the on-chip Ag/AgCl RE), remaining within the electrochemical potential window of the system. An initial slight peak then pronounced wave at approximately −0.5 V was visible, and was absent after purging oxygen from the PBS solution using nitrogen (Fig. 3b). This indicates that the peak was caused by oxygen reduction at the WE surface, and the wave by diffusion limited oxygen reduction through the Nafion membrane. These results confirmed that the annealed Nafion membrane was

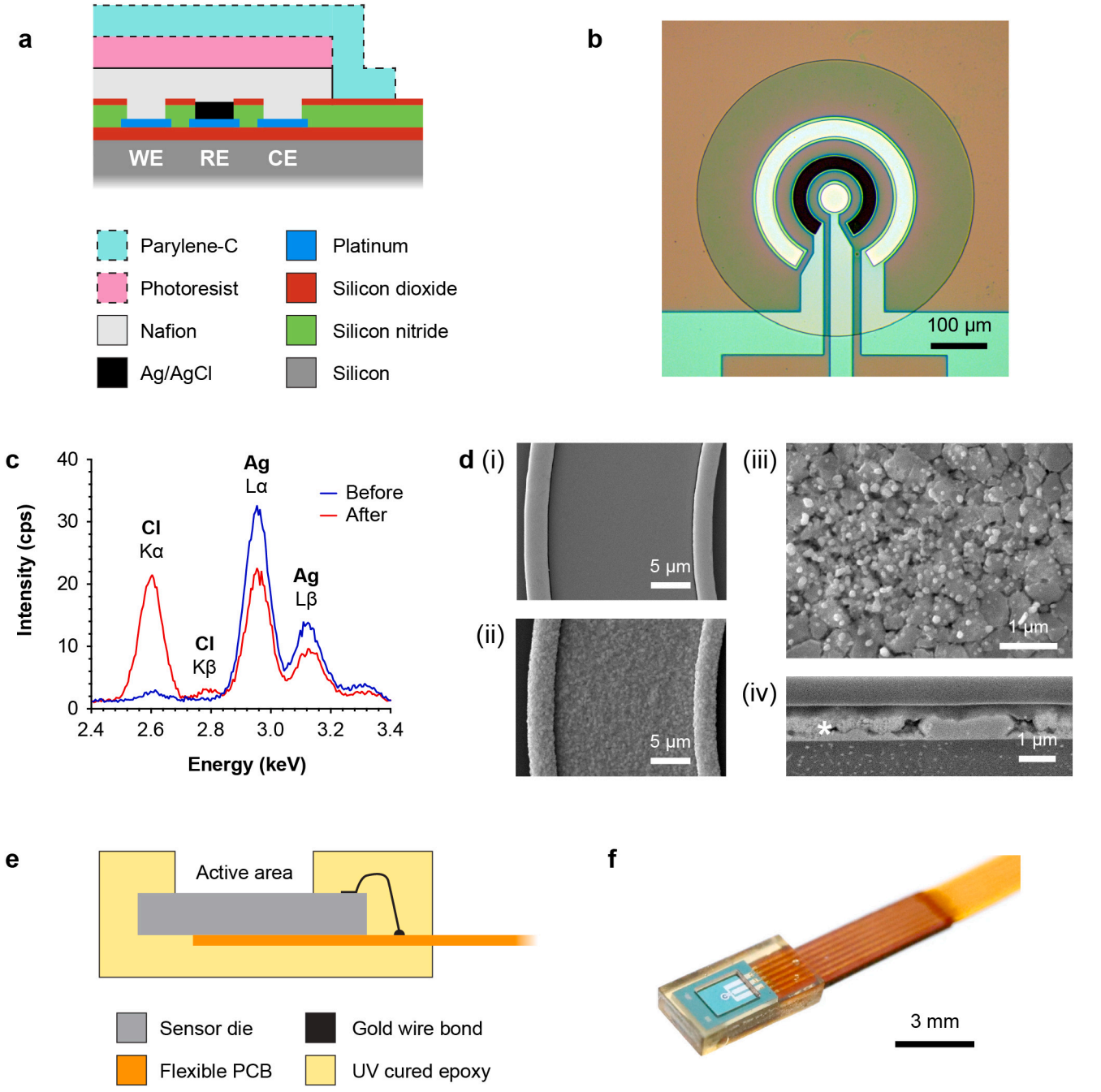

Fig. 2. Sensor electrodes and packaging. (a) Schematic cross-section through the sensor active area showing the electrode layer stack and Nafion membrane, with protective sacrificial Parylene-C and photoresist layers (dashed outline) in place prior to packaging (not to scale). (b) Photograph of a microfabricated sensor die, after removal of protective layers, showing the physical arrangement of the WE (centre disc), RE (dark middle ring), CE (outer ring), and Nafion membrane (darker circle covering electrodes). (c) Typical EDX spectra of the RE surface obtained before and after chloridisation. Characteristic X-ray energy peaks corresponding to Ag and Cl are indicated. Spectra shown are the mean of three areas on the same device. Similar results were obtained from four devices. (d) SEM images of the RE surface before (i), and after (ii) chloridisation, at higher magnification after chloridisation (iii), and in cross-section (iv) after deposition of Nafion and protective layers (asterisk indicates Ag/AgCl layer, with layers of Nafion above and silicon below). (e) Schematic cross-section through the assembled sensor packaging showing the sensor connected to a flexible PCB and encapsulated in UV cured epoxy (not to scale). (f) Photograph of a packaged sensor and its flexible PCB lead.

capable of permitting oxygen and small ion transport. Additional peaks were frequently evident in the PBS CV at approximately +0.07 V and −0.15 V, which are characteristic of silver chloride and may indicate some mechanical transfer from the RE onto the WE surface during fabrication. However, these were well separated in potential from the oxygen reduction reaction, and were not observed to interfere with its position or magnitude.

We next performed chronoamperometry (CA) at −0.5 V (vs the on-chip Ag/AgCl RE) for 20 s. In air-saturated PBS the WE current showed an expected initial transient related to capacitive charging, reduction of oxygen, and formation of oxygen diffusion gradients at its surface (consistent with the CV peak). This was followed by the development of an approximately steady-state current caused by diffusion-controlled oxygen reduction (consistent with the CV wave). In nitrogen purged PBS the steady-state current was markedly decreased, again consistent with the CV results and identifying the current as oxygen reduction

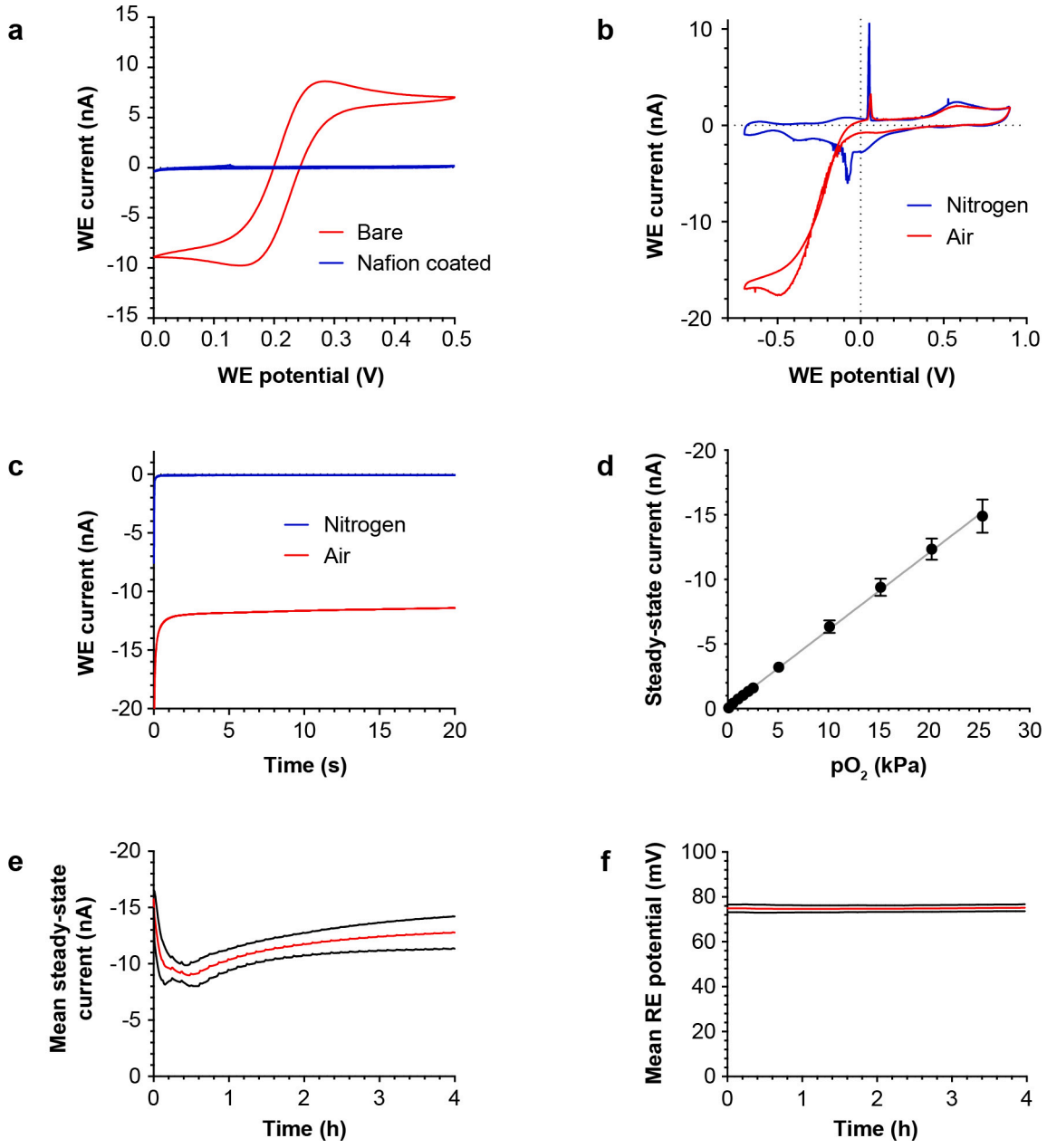

Fig. 3. Sensor characterisation. (a) Typical CV scans of bare and Nafion coated sensors in a solution of 1 mM potassium ferricyanide and 1 mM potassium ferrocyanide, in a 100 mM potassium chloride supporting electrolyte. Similar results were obtained from six sensors with an intact Nafion membrane, and two sensors with bare electrodes. WE potential was set against an external Ag|AgCl|KCl (3 M) RE for both types of sensor. (b) Typical CV scans of a sensor in PBS saturated with air or after purging with nitrogen. The WE potential was set against the on-chip Ag/AgCl RE. Similar results were obtained from three sensors. (c) Typical CA traces from a sensor in PBS saturated with air or after purging with nitrogen, following a potential step to −0.5 V (vs on-chip Ag/AgCl RE). Similar results were obtained from four sensors. (d) Mean WE steady-state current at −0.5 V (vs on-chip Ag/AgCl RE) in PBS, measured over a range of dissolved oxygen concentrations. At each oxygen concentration 4 repeat measurements were made from each sensor (n = 4 sensors). Error bars show SD between sensors. (e) Stability of the mean WE steady-state current, measured by CA at −0.5 V (vs on-chip Ag/AgCl) in air saturated PBS. Measurements were made for 20 s, with 20 s gaps between recordings, repeated continuously (n = 8 sensors). (f) Stability of the mean on-chip RE potential (vs external Ag/AgCl) of the same sensors, measured after every tenth CA cycle for 10 s (n = 8 sensors). In both e & f the mean measurement is shown in red, and the black bands represent SD between sensors.

(Fig. 3c). To investigate the linearity of the oxygen response, its partial pressure (pO_2) in solution was varied from 0.1 to 25.3 kPa (equivalent to 0.1 to 25.0% of atmospheric pressure) by sparging with a range of oxygen/nitrogen mixtures. A greater sampling resolution was used in the lower range relevant to biological tissue. The sensor response to oxygen was quantified using the mean current over the final 5 s of a 20 s CA recording, as the steady-state was well established by this point. Linear regression showed a proportional relationship between the steady-state current and oxygen concentration (r^2 = 0.991), with a fitted sensitivity of −0.595 ± 0.009 nA/kPa and a statistically insignificant offset of −0.143 ± 0.100 nA (Fig. 3d). Quantification of oxygen concentration as the mean steady-state CA current at −0.5 V (vs on-chip Ag/AgCl RE), averaged over the final 5 s of a 20 s recording, was therefore adopted for all further measurements. Together these results show that the sensor output varies directly with oxygen concentration as expected, with insignificant offset due to unrelated currents at the WE.

To investigate the performance of the packaged sensors over time, oxygen measurements using CA were repeatedly performed in air-saturated PBS. The RE potential was also recorded from the same devices

against an external Ag/AgCl RE in the rest periods between CA measurements. Over 4 h the sensors gave an average steady-state current of −11.4 ± 0.8 nA (n = 8 sensors) in air-saturated PBS (Fig. 3e). To quantify individual sensor stability, the coefficient of variance (CoV, defined as [SD / Mean] × 100%) of the output from each sensor was also calculated, and gave a mean CoV of 12.2% over the 4 h measurement period (n = 8 sensors). The RE potential remained very stable over the same period (Fig. 3f), with an average value of +74.8 ± 1.5 mV (n = 8 sensors), and a mean CoV of only 0.33% (n = 8 sensors). The measurements were then continued until sensor failure to investigate their lifetime. Ultimately the first element of the sensor to fail was the RE. A change in RE potential typically occurred quite suddenly, leading in turn to unreliable CA oxygen measurements as the WE bias could not be accurately set (Fig. S3). A difference in RE potential of more than ± 50 mV from its initial value was defined as the failure point, and gave a mean time-to-failure of 23.3 h (range 5.1–64.5 h, n = 8 sensors).

We next systematically explored how sensor performance may be affected by exposure to the *in vivo* environment. To test whether the sensor was susceptible to protein biofouling, we recorded oxygen measurements from sensors in air-saturated PBS containing bovine serum albumin (BSA). This is a well characterised, water soluble protein, commonly used as a surrogate to model biofouling. Air-saturated PBS alone was used as a control. Sensors exposed to BSA showed a significant decrease in steady-state WE current after 24 h (Fig. 4a), suggesting that biofouling due to non-specific protein adsorption may lower the sensitivity of the Nafion coated sensors. We then tested the interference effect of common electroactive compounds (hydrogen peroxide, urate, ascorbate, and paracetamol) that are found *in vivo* and known to affect electrochemical measurements. Compounds were dissolved in air-saturated PBS, and oxygen measurements were sequentially performed in each solution in a randomised order. When compared to PBS alone, we found that physiological concentrations of hydrogen peroxide (3 μM), ascorbate (45 μM), and paracetamol (100 μM) all had no significant effect on the steady-state WE current, while urate (375 μM) caused a significant decrease in the magnitude of the current (Fig. 4b).

As the sensor was designed to be surgically implanted and remain in place during a course of radiotherapy, we finally tested whether it was adversely affected by sterilisation or irradiation. Ethylene oxide gas was used to sterilise the sensors as it is routinely used to sterilise medical equipment. Irradiation was performed under a clinical radiotherapy beam, using a dose of four fractions of 6 Gy. This fraction size is within the upper range typically delivered in human clinical use [42], and matches that used in previous work involving a sheep lung cancer model [43]. Following these treatments, the on-chip RE potential was unchanged (Fig. 5a), and the Nafion membrane was still impermeable to ferri/ferrocyanide anions (Fig. 5b), indicating that its physical integrity and selectivity had not been compromised. Using CV in PBS we observed that the expected oxygen reduction features were still evident (Fig. 5c), and that the corresponding CA steady-state oxygen current at −0.5 V (vs the on-chip Ag/AgCl RE) was also unchanged (Fig. 5d), showing that the electrodes were undamaged.

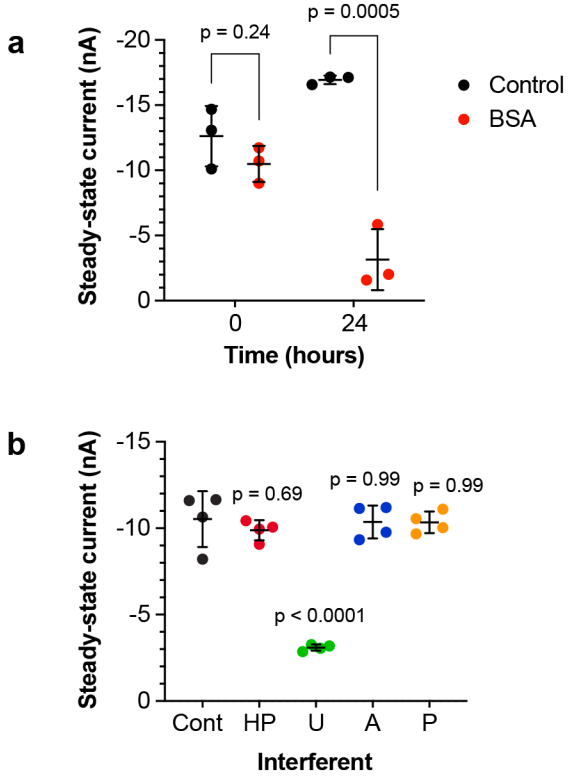

Fig. 4. Effect of protein biofouling and interferents on sensor performance. (a) Mean WE steady-state current at −0.5 V (vs on-chip Ag/AgCl RE) in PBS (Control) or 35 mg/mL BSA in PBS (BSA), showing effect of protein biofouling at the start (0 h) and end (24 h) of the experiment (n = 3 sensors for each condition). Error bars represent SD between sensors. (b) Mean WE steady-state current at −0.5 V (vs on-chip Ag/AgCl RE) in PBS (Cont), and PBS containing 3 μM hydrogen peroxide (HP), 375 μM urate (U), 45 μM ascorbate (A), or 100 μM paracetamol (P) (n = 4 sensors for each treatment). Error bars represent SD between sensors. Statistical comparisons were made to the PBS (Control) condition.

3.3. *In vivo* validation

Bench characterisation showed that the sensor could report oxygen concentration in solution effectively over many hours. We therefore next tested whether the sensor was sufficiently robust to operate *in vivo* and detect dynamic changes in tissue oxygenation. We used a novel clinically relevant ovine model of lung cancer [38], developed specifically for this project. Tumours in three sheep with naturally occurring pre-clinical ovine pulmonary adenocarcinoma were implanted with either one sensor (Cases F1 & F2) or two sensors (Case F3). Each sensor was implanted under anaesthesia using a Jamshidi needle using CT guidance (Fig. 6a,b). The sheep were initially maintained at a target FiO_2 of 1.00, then exposed to a protocol of mild graded tissue hypoxia by stepping their FiO_2 down to 0.50 and then 0.21, before being returned to an FiO_2 of 1.00 (Fig. 6c). Arterial blood analysis showed the expected changes in oxygenation (Fig. 6d and Fig. S4a), while other relevant physiological variables did not change significantly (Fig. S4b-e). During the protocol, measurements were repeatedly made from the sensors using CA and all gave measurable real-time outputs (Fig. S5). Interestingly, there was substantial variability between cases and so readings from each sensor were analysed independently. Both sensors in Case F3 showed low initial currents which did not respond to changes in FiO_2, while the sensors in Cases F1 and F2 showed a relatively higher initial current with partially reversible decreases at lower FiO_2 values and a decrease following euthanasia (Fig. 6e). These differences reflect the expected heterogeneity of tumour hypoxia and oxygen responsiveness.

To confirm that the sensors survived the tumour implantation procedure they were recovered following euthanasia, gently rinsed in water, and tested. Their surfaces showed the presence of some contamination (Fig. 7a), likely derived from lung tissue at the implant site. CV in air-saturated PBS showed the expected presence of oxygen reduction at negative potentials for all sensors (Fig. 7b). The mean steady-state CA current showed greater variability between sensors post-implantation but was not significantly different to its pre-implantation value (Fig. 7c). Together these results demonstrate that the packaged sensor is sufficiently physically robust to remain functional throughout a clinically realistic implantation procedure.

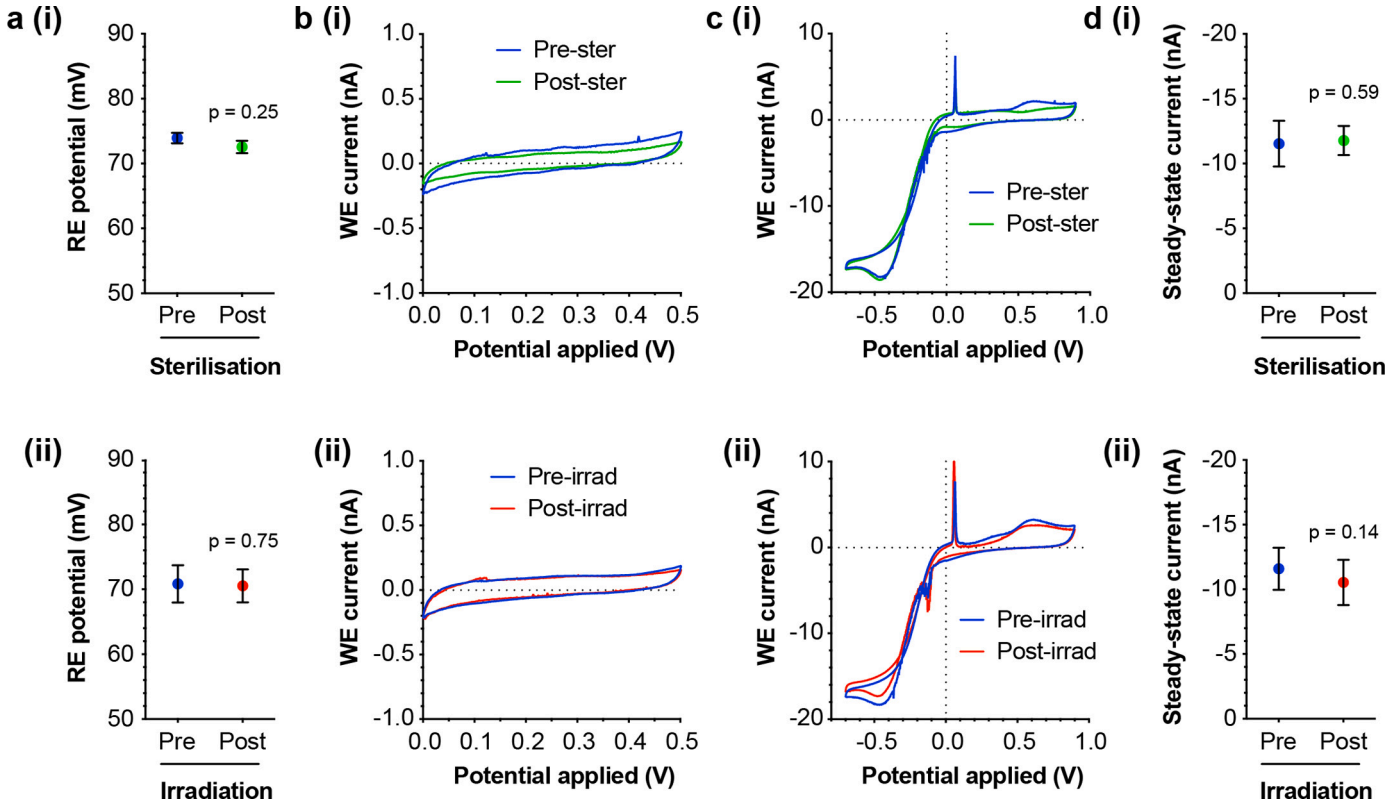

Fig. 5. Robustness to sterilisation and irradiation. Sensors were either (i) sterilised with ethylene oxide, or (ii) exposed to four radiotherapy fractions of 6 Gy. Measurements are shown pre- and post-treatment. (a) Sensor RE potential measured against an external Ag|AgCl|KCl (3 M) RE (n = 3 sensors for each treatment). Error bars represent SD between sensors. (b) Typical CV scans in a solution of 1 mM potassium ferricyanide and 1 mM potassium ferrocyanide, in a 100 mM potassium chloride supporting electrolyte. Similar results were obtained from three sensors for each treatment. WE potential was set against an external Ag|AgCl|KCl (3 M) RE. (c) Typical CV scans in PBS saturated with air. Similar results were obtained from three sensors for each treatment. The WE potential was set against the on-chip Ag/AgCl RE. (d) Mean WE steady-state current at −0.5 V (vs on-chip Ag/AgCl RE) in PBS (n = 4 sensors for each treatment). Error bars represent SD between sensors.

4. Discussion

Together, this work describes a microfabricated electrochemical oxygen sensor that is suitable for implantation, and demonstrates its functionality and relevance for real-time measurement in a realistic clinical environment. The wafer-level microfabrication approach we adopted for producing the sensor has two advantages. Firstly, it enables the sensor to be mass manufacturable with high repeatability through use of standard industrial tools and tight process control, and minimises costly and potentially inconsistent die-level processing. These features will be very important for gaining medical regulatory approval, as sensor accuracy and repeatability are essential for making safe clinical decisions. Secondly, it will enable our future aim of post-processing the oxygen sensor architecture on CMOS wafers to produce a device that contains integrated potentiostat instrumentation and wireless power and communication electronics. This will also allow the volume of the device to be minimised by eliminating dependence on the existing assembly and packaging elements required for connection to external instrumentation.

The sensor membrane is a defining component of the Clark electrode, separating its bare electrodes from the chemically complex surrounding fluid. Our membrane was fabricated from Nafion, a perfluorinated cation exchange resin that is both oxygen permeable and can conduct protons between electrodes to support the electrochemical reactions [17]. Wafer-level spin coating was used to deposit the Nafion membrane, followed by heat annealing. Annealing increases Nafion solvent resistance [44], improving integration with standard wet microfabrication processes and improving its stability in aqueous environments. Furthermore, it also improves Nafion proton conductivity and electrochemical surface area [45,46], tensile strength [45], and the lifetime of implanted Nafion coated Ag/AgCl reference electrodes [35]. Photolithographic patterning and dry etching were then used to accurately define the membrane areas across the wafer. Together this novel combination of processes significantly improved manufacturability compared to previously described microfabricated oxygen sensors that used die-level drop cast Nafion membranes that were not annealed [21,23,28].

Selectivity of the Clark sensor membrane is important for sensor accuracy. The polymer backbone of Nafion carries negatively charged sulphonate groups that can electrostatically exclude anionic species, and the nanometer scale of its hydrophillic pores causes size exclusion of large ions [17]. Consistent with these effects, we observed that our membrane blocked ferricyanide ($[Fe(CN)_6]^{3-}$) and ferrocynanide ($[Fe(CN)_6]^{4-}$) ions from reacting at the WE. In addition, no significant interference was observed from physiological concentrations of ascorbate, hydrogen peroxide, or paracetamol. We found that urate decreased the measured current from the sensor, indicating that it may interfere with oxygen measurements. There is conflicting literature regarding Nafion permeability to urate, with several reports showing that Nafion improves selectivity for catecholamine neurotransmitter measurements in the presence of urate [47], while others have shown that it can be used to block ascorbate and allow selective measurement of urate [48–50]. Our data suggest that the Nafion sensor membrane is permeable to urate, likely in its protonated uric acid form as it would otherwise be electrostatically excluded, and may become deposited within the hydrated pores limiting mass transport.

An additional function of the membrane was to prevent electrode biofouling. Nafion is generally thought to reduce biofouling [33,34],

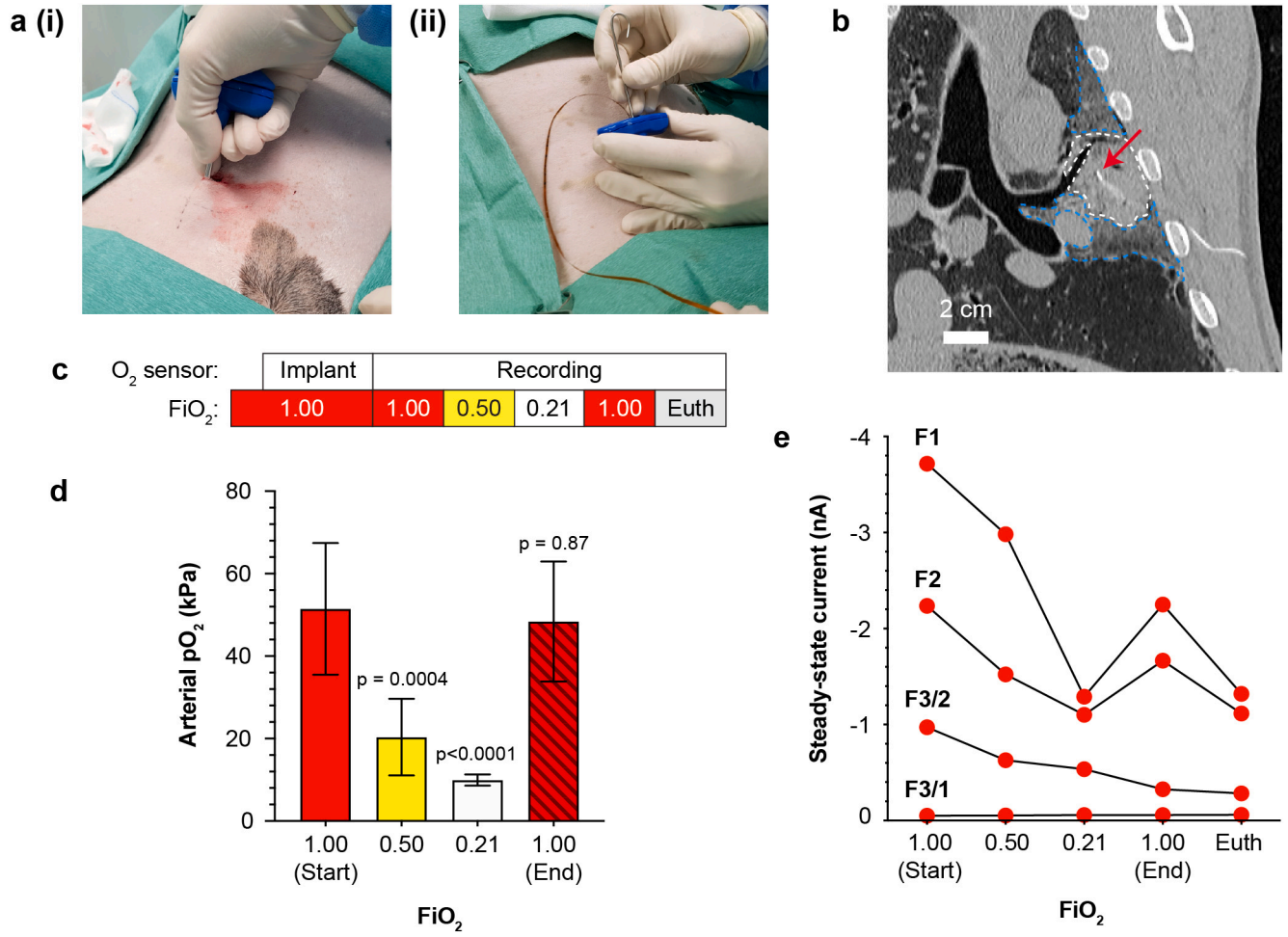

Fig. 6. Surgical implantation and sensor operation in lung tumour. (a) Photographs showing the procedure for surgical implantation of a sensor. (i) Insertion of a Jamshidi needle through the chest wall and into the lung tumour, (ii) introduction of the sensor and lead wire down the bore of the needle, and ejection from the needle into tumour tissue using a metal rod. (b) Typical thoracic coronal CT image (Case F1) following implantation showing sensor location (red arrow) within tumour tissue (white dashed outline). The tumour is surrounded by areas consistent in appearance with neoplastic foci or secondary pneumonia (blue dashed outline). (c) Schematic of sensor implantation and FiO_2 sequence. (d) Arterial blood oxygen partial pressure at the end of each FiO_2 step (n = 4 protocol repeats, from three animals). Error bars represent SD between repeats. (e) Mean sensor output at each FiO_2 level, averaged over the final 5 min of the FiO_2 step. The output from each sensor is plotted independently (one sensor in each of Cases F1 & F2, two sensors in Case F3).

however we observed that exposure of the sensor to a solution of BSA caused a significant decrease in its oxygen sensitivity over 24 h. This is likely to be due to surface adsorption of protein, since BSA will be size excluded from the Nafion membrane pores. Biofouling may partly account for the measured variability in the performance of sensors that were recovered at post-mortem following tumour implantation, and it will need to be addressed before translation to human clinical trials.

An essential component of any electrochemical sensor is the RE,

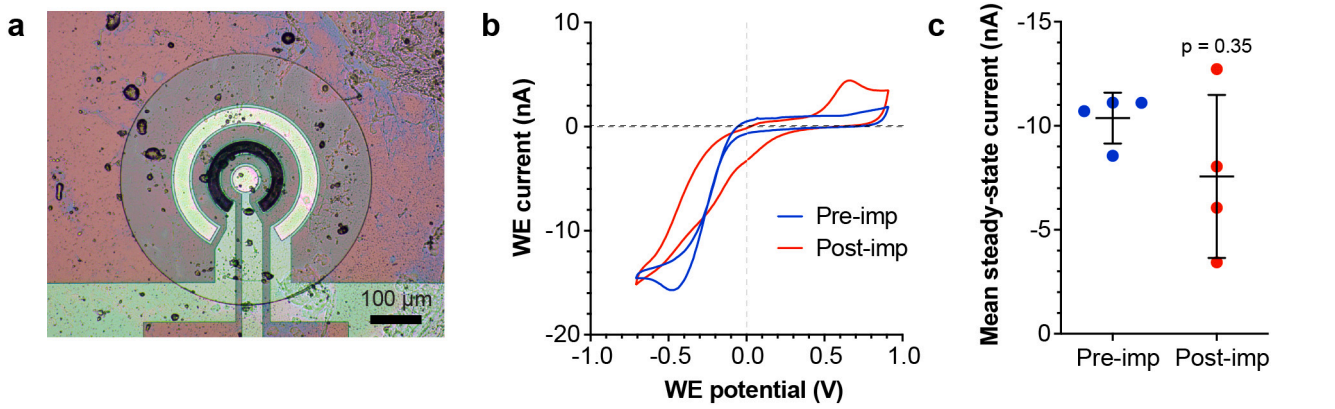

Fig. 7. Sensor function post-implantation. (a) Photograph showing typical sensor surface contamination following recovery at post-mortem. (b) Typical pre- and post-implantation CV scans in PBS saturated with air. Similar results were obtained from four sensors. The WE potential was set against the on-chip Ag/AgCl RE. (c) Mean CA steady-state current at −0.5 V (vs on-chip Ag/AgCl RE) in PBS (n = 4 sensors). Error bars represent SD between sensors.

necessary to provide the potential against which the WE potential is measured or set. Key parameters of RE performance are potential stability, sensitivity to environmental variables, and lifetime. Our Nafion coated Ag/AgCl RE successfully provided a sufficiently stable potential to enable accurate measurements to be made both *in vitro* and *in vivo*. Its potential was set by the surrounding chloride concentration in a typical Nerstian response, as others have previously observed for reference electrodes without a defined internal electrolyte [16]. This is not expected to cause problems in an implanted setting, as chloride concentration is under tight homeostatic control, with a typical range of 97–107 mM in human plasma [51]. During long-term testing, we typically saw failure (defined by a sudden large potential change) of the RE in less than a day, leading to unreliable measurements. This may reflect mechanical instability of the AgCl layer, or exhaustion of either Ag or AgCl. The failure origin will be investigated, since the short lifetime of our sensor remains a limitation that will need to be improved for clinical applications.

The sensor was designed from the start for implantation, and so all the outward facing materials were selected for their established biocompatibility, including silicon dioxide [52–54], Nafion [55–57], and Epotek OG116–31 epoxy resin. We have recently demonstrated that implantation of these sensor materials does not cause changes in tumour pathology [58], which will be essential for clinical deployment. Others have previously shown that a large implanted Ag/AgCl RE can cause local toxicity. To minimise this risk, we used a Nafion RE coating which is known to reduce the toxicity of implanted Ag/AgCl electrodes [35]. The PCB insulation was manufactured from polyimide, which is already commonly used for encapsulating and insulating implantable medical devices [59].

To validate the sensor in tumour tissue we used an ovine pulmonary adenocarcinoma model. This model has high translational value, as it closely reflects both human lung cancer biology [60], and the surgical methods used for tumour management such as trans-thoracic needle biopsy [38]. The experiments described here represent the first use of this novel preclinical model for validation of an implantable sensor in tumour tissue. Oxygen sensor readings obtained from the implanted sensors showed substantial variation between cases, consistent with a poorly perfused hypoxic tumour environment at both sensor locations in Case F3, but better perfusion and responsiveness to changes in blood oxygenation at the sensor locations in Cases F1 and F2. This underlines the known spatial heterogeneity of hypoxia that is found in solid tumours [1]. Interestingly, our results are also consistent with a previous human lung cancer study which showed highly variable responsiveness of tumour hypoxia to breathing 95% oxygen as a potential radiotherapy sensitising technique [61].

Hypoxia is also a feature of many other pathological states. These include chronic conditions such as non-healing wounds [62], while acute disruption occurs in life-threatening conditions such as hypovolaemic, cardiogenic and septic shock [63], and following traumatic brain injury [64]. Our minimally invasive technique for continuously measuring tissue oxygenation could therefore also be a valuable tool for clinicians involved in the treatment and management of a broad range of other medical conditions. We are currently engaged in further implantation studies to determine whether the sensor is suitable for post-surgical monitoring of intestinal tissue oxygenation following resection and anastomosis [65].

5. Conclusion

Hypoxia is distributed heterogeneously within solid tumours, and can vary over time. It inhibits the effectiveness of radiotherapy treatment, arguing for tumour oxygenation status to be included in radiotherapy planning. Here, we describe a miniature implantable sensor for continuous real-time monitoring of tumour hypoxia. The fabrication process comprises only CMOS compatible wafer-level processing techniques, and produces a novel layer stack suitable for integration with biocompatible epoxy encapsulation. The sensor gave a linear response to oxygen, although it showed some susceptibility to biofouling and interference by urate, and its lifetime was limited to between hours and days by failure of the on-chip RE. We showed that the packaged sensor was sufficiently robust to function over this timescale within a tumour using a translational model of lung cancer, and demonstrated measurement of dynamic changes in tissue oxygenation *in vivo*. Our future work will focus on addressing the limitations of sensor lifetime and selectivity, alleviating the effects of biofouling, and ultimately achieving full integration with on-chip instrumentation and wireless power and communications.

Author contributions

AFM, DJA, AJW, ARM & IHK conceived the approach. CD, JRKM, EOB, AT & EG-F designed and fabricated the sensors. JRKM, CD, EOB & MEG performed the sensor characterisation experiments. MMP performed the sensor irradiation. MEG, AD, MS & MAP developed methodology for *in vivo* recording. MEG, PS, SNG, RG, REC & DJA developed methodology for the lung tumour implantation experiments and performed the sheep *in vivo* work. JRKM & ARM analysed the data. AFM, DJA, AJW, IU, ARM, SS, JGT, SM, MAP, MS & REC supervised the experiments. JRKM & MEG wrote the manuscript, and it was reviewed and edited by all the authors.

Declaration of Competing Interest

The authors declare no competing interests.

Acknowledgements

This work was supported by funding from the UK Engineering and Physical Sciences Research Council through the Implantable Microsystems for Personalised Anti-Cancer Therapy (IMPACT) programme grant (EP/K034510/1), from a project grant from Bowel and Cancer Research UK, and from a Wellcome Trust Biomedical Resource Grant to the Wellcome Trust Critical Care Laboratory for Large Animals (104972/Z/14/Z). We are grateful to S. Ramsay and R. Blair for their technical assistance during sensor fabrication; E. MacDonald for constructing the O_2/N_2 gas mixing apparatus used for sensor characterisation; I. Schmueser for advice on electrochemistry; E. Kay and H. Porter for assistance and advice during sensor irradiation testing; J. Nixon, P. Tennant and A. Ritchie for sheep husbandry and sensor sterilisation; and L. Grant for CT imaging. Sheep OPA cases were obtained by P. Scott (Capital Veterinary Services).

Appendix A. Supplementary data

Supplementary data to this article can be found online at https://doi.org/10.1016/j.sbsr.2020.100375.

References

[1] M. Hockel, P. Vaupel, Tumor hypoxia: definitions and current clinical, biologic, and molecular aspects, JNCI 93 (4) (2001) 266–276, https://doi.org/10.1093/jnci/93.4.266.

[2] M.W. Dewhirst, Y. Cao, B. Moeller, Cycling hypoxia and free radicals regulate angiogenesis and radiotherapy response, Nat. Rev. Cancer 8 (6) (2008) 425–437, https://doi.org/10.1038/nrc2397.

[3] L.H. Gray, A.D. Conger, M. Ebert, S. Hornsey, O.C.A. Scott, The concentration of oxygen dissolved in tissues at the time of irradiation as a factor in radiotherapy, Br. J. Radiol. 26 (312) (1953) 638–648, https://doi.org/10.1259/0007-1285-26-312-638.

[4] P. Vaupel, A. Mayer, Hypoxia in cancer: significance and impact on clinical outcome, Cancer Metastasis Rev. 26 (2) (2007) 225–239, https://doi.org/10.1007/s10555-007-9055-1.

[5] S.M. Bentzen, V. Gregoire, Molecular imaging–based dose painting: a novel paradigm for radiation therapy prescription, Semin. Radiat. Oncol. 21 (2) (2011) 101–110, https://doi.org/10.1016/j.semradonc.2010.10.001.

[6] S.A. Bhide, C.M. Nutting, Recent advances in radiotherapy, BMC Med. 8 (1) (2010) 25, , https://doi.org/10.1186/1741-7015-8-25.

[7] E.M. Hammond, M.C. Asselin, D. Forster, J.P. O'Connor, J.M. Senra, K.J. Williams, The meaning, measurement and modification of hypoxia in the laboratory and the clinic, Clin. Oncol. 26 (5) (2014) 277–288, https://doi.org/10.1016/j.clon.2014.02.002.

[8] B. Epel, M. Kotecha, H.J. Halpern, In vivo preclinical cancer and tissue engineering applications of absolute oxygen imaging using pulse EPR, J. Magn. Reson. 280 (2017) 149–157, https://doi.org/10.1016/j.jmr.2017.04.017.

[9] P. Vaupel, M. Höckel, A. Mayer, Detection and characterization of tumor hypoxia using pO_2 Histography, Antioxid. Redox Signal. 9 (8) (2007) 1221–1236, https://doi.org/10.1089/ars.2007.1628.

[10] J.R.K. Marland, et al., Implantable microsystems for personalised anticancer therapy, CMOS Circuits for Biological Sensing and Processing, 2018, pp. 259–286, , https://doi.org/10.1007/978-3-319-67723-1_11.

[11] T. Ikegwuonu, G. Haddow, J. Tait, A.F. Murray, I.H. Kunkler, Horizon scanning implanted biosensors in personalising breast cancer management: first pilot study of breast cancer patients views, Health Sci. Rep. 1 (4) (2018) e30, https://doi.org/10.1002/hsr2.30.

[12] H.L. Danneel, Über den durch Diffundierende Gase Hervorgerufenen Reststrom, Zeitschrift für Elektrochemie 4 (9) (1897) 227–242, https://doi.org/10.1002/bbpc.18970040903.

[13] L.C. Clark, Monitor and control of blood and tissue oxygen tension, Trans. Am. Soc. Artif. Intern. Organs 2 (1956) 41–48.

[14] A.M. Gómez–Marín, E.A. Ticianelli, A reviewed vision of the oxygen reduction reaction mechanism on Pt-based catalysts, Curr. Opin. Electrochem. 9 (2018) 129–136, https://doi.org/10.1016/j.coelec.2018.03.008.

[15] J.W. Severinghaus, P.B. Astrup, History of blood gas analysis. IV. Leland Clark's oxygen electrode, J. Clin. Monit. 2 (2) (1986) 125–139, https://doi.org/10.1007/bf01637680.

[16] M.W. Shinwari, D. Zhitomirsky, I.A. Deen, P.R. Selvaganapathy, M.J. Deen, D. Landheer, Microfabricated reference electrodes and their biosensing applications, Sensors 10 (3) (2010) 1679–1715, https://doi.org/10.3390/s100301679.

[17] A. Kusoglu, A.Z. Weber, New insights into perfluorinated sulfonic-acid ionomers, Chem. Rev. 117 (3) (2017) 987–1104, https://doi.org/10.1021/acs.chemrev.6b00159.

[18] T. Xiao, et al., In vivo monitoring of oxygen fluctuation simultaneously at multiple sites of rat cortex during spreading depression, Anal. Chem. 90 (22) (2018) 13783–13789, https://doi.org/10.1021/acs.analchem.8b04348.

[19] J. Kieninger, et al., Sensor access to the cellular microenvironment using the sensing cell culture flask, Biosensors (Basel) 8 (2) (2018) 1–11, https://doi.org/10.3390/bios8020044.

[20] S.M. Bonk, et al., Design and characterization of a Sensorized microfluidic cell-culture system with electro-thermal micro-pumps and sensors for cell adhesion, oxygen, and pH on a glass Chip, Biosensors (Basel) 5 (3) (2015) 513–536, https://doi.org/10.3390/bios5030513.

[21] W.P. Chan, et al., A monolithically integrated pressure/oxygen/temperature sensing SoC for multimodality intracranial Neuromonitoring, IEEE J. Solid-St Circ 49 (11) (2014) 2449–2461, https://doi.org/10.1109/Jssc.2014.2345754.

[22] Y. Eminaga, M. Brischwein, J. Wiest, J. Clauss, S. Becker, B. Wolf, Self calibration of a planar dissolved oxygen sensor, Sensors Actuators B Chem. 177 (2013) 785–791, https://doi.org/10.1016/j.snb.2012.11.104.

[23] P. Wang, Y. Liu, H.D. Abruna, J.A. Spector, W.L. Olbricht, Micromachined dissolved oxygen sensor based on solid polymer electrolyte, Sensor Actuat B-Chem 153 (1) (2011) 145–151, https://doi.org/10.1016/j.snb.2010.09.075.

[24] C.C. Wu, H.N. Luk, Y.T.T. Lin, C.Y. Yuan, A Clark-type oxygen chip for in situ estimation of the respiratory activity of adhering cells, Talanta 81 (1–2) (2010) 228–234, https://doi.org/10.1016/j.talanta.2009.11.062.

[25] J. Park, Y.K. Pak, J.J. Pak, A microfabricated reservoir-type oxygen sensor for measuring the real-time cellular oxygen consumption rate at various conditions, Sensors Actuators B Chem. 147 (1) (2010) 263–269, https://doi.org/10.1016/j.snb.2010.03.069.

[26] C.C. Wu, T. Yasukawa, H. Shiku, T. Matsue, Fabrication of miniature Clark oxygen sensor integrated with microstructure, Sensor Actuat B-Chem 110 (2) (2005) 342–349, https://doi.org/10.1016/j.snb.2005.02.014.

[27] M. Brischwein, E.R. Motrescu, E. Cabala, A.M. Otto, H. Grothe, B. Wolf, Functional cellular assays with multiparametric silicon sensor chips, Lab Chip 3 (4) (2003) 234–240, https://doi.org/10.1039/b308888j.

[28] G.W. McLaughlin, K. Braden, B. Franc, G.T.A. Kovacs, Microfabricated solid-state dissolved oxygen sensor, Sensor Actuat B-Chem 83 (1–3) (2002) 138–148, https://doi.org/10.1016/S0925-4005(02)00021-7.

[29] H. Suzuki, T. Hirakawa, S. Sasaki, I. Karube, An integrated module for sensing pO_2, pCO_2, and pH, Anal. Chim. Acta 405 (1–2) (2000) 57–65, https://doi.org/10.1016/S0003-2670(99)00748-5.

[30] H.X. Zhu, T.C. Lo, R. Lenigk, R. Renneberg, Fabrication of a novel oxygen sensor with CMOS compatible processes, Sensors Actuators B Chem. 46 (2) (1998) 155–159, https://doi.org/10.1016/S0925-4005(98)00044-6.

[31] H. Yin, X. Mu, H. Li, X. Liu, A.J. Mason, CMOS monolithic electrochemical gas sensor microsystem using room temperature ionic liquid, IEEE Sensors J. 18 (19) (2018) 7899–7906, https://doi.org/10.1109/jsen.2018.2863644.

[32] J.R.K. Marland, et al., Optimization of Nafion polymer electrolyte membrane design and microfabrication, IEEE Trans. Semicond. Manuf. 33 (2) (2020) 196–201, https://doi.org/10.1109/TSM.2020.2983875.

[33] G. Rocchitta, et al., Enzyme biosensors for biomedical applications: strategies for safeguarding analytical performances in biological fluids, Sensors 16 (6) (2016) 780, https://doi.org/10.3390/s16060780.

[34] N. Wisniewski, M. Reichert, Methods for reducing biosensor membrane biofouling, Colloid Surface B 18 (3–4) (2000) 197–219, https://doi.org/10.1016/S0927-7765(99)00148-4.

[35] F. Moussy, D.J. Harrison, Prevention of the rapid degradation of subcutaneously implanted Ag/AgCl reference electrodes using polymer-coatings, Anal. Chem. 66 (5) (1994) 674–679, https://doi.org/10.1021/ac00077a015.

[36] P.R. Scott, M.P. Dagleish, C. Cousens, Development of superficial lung lesions monitored on farm by serial ultrasonographic examination in sheep with lesions confirmed as ovine pulmonary adenocarcinoma at necropsy, Ir. Vet. J. 71 (1) (2018) 23, , https://doi.org/10.1186/s13620-018-0134-0.

[37] C. Cousens, P.R. Scott, Assessment of transthoracic ultrasound diagnosis of ovine pulmonary adenocarcinoma in adult sheep, Vet. Rec. 177 (14) (2015) 366, https://doi.org/10.1136/vr.103298.

[38] M.E. Gray, et al., A novel translational ovine pulmonary adenocarcinoma model for human lung cancer, Front. Oncol. 9 (2019) 534, https://doi.org/10.3389/fonc.2019.00534.

[39] C. Dunare, et al., Test structures for characterising the silver chlorination process during integrated Ag/AgCl reference electrode fabrication, 2019 International Conference of Microelectronic Test Structures (ICMTS), 2019, https://doi.org/10.1109/ICMTS.2019.8730966.

[40] E.O. Blair, et al., Test structures for the characterisation of sensor packaging technology, 2017 International Conference of Microelectronic Test Structures (ICMTS), 2017, pp. 1–6, , https://doi.org/10.1109/icmts.2017.7954279.

[41] T. Luo, S. Abdu, M. Wessling, Selectivity of ion exchange membranes: a review, J. Membr. Sci. 555 (2018) 429–454, https://doi.org/10.1016/j.memsci.2018.03.051.

[42] M.V. Williams, N.D. James, E.T. Summers, A. Barrett, D.V. Ash, National survey of radiotherapy fractionation practice in 2003, Clin. Oncol. 18 (1) (2006) 3–14, https://doi.org/10.1016/j.clon.2005.10.002.

[43] D. Collie, et al., Nebulisation of synthetic lamellar lipids mitigates radiation-induced lung injury in a large animal model, Sci. Rep. 8 (1) (2018) 13316, , https://doi.org/10.1038/s41598-018-31559-3.

[44] L.A. Zook, J. Leddy, Density and solubility of nafion: recast, annealed, and commercial films, Anal. Chem. 68 (21) (1996) 3793–3796, https://doi.org/10.1021/ac960604e.

[45] X.Y. Ding, S. Didari, T.F. Fuller, T.A.L. Harris, Effects of annealing conditions on the performance of solution cast Nafion membranes in fuel cells, J. Electrochem. Soc. 160 (8) (2013) F793–F797, https://doi.org/10.1149/2.034308jes.

[46] H.Y. Jung, K.Y. Cho, Y.M. Lee, J.K. Park, J.H. Choi, Y.E. Sung, Influence of annealing of membrane electrode assembly (MEA) on performance of direct methanol fuel cell (DMFC), J. Power Sources 163 (2) (2007) 952–956, https://doi.org/10.1016/j.jpowsour.2006.09.047.

[47] J.A. Ribeiro, P.M.V. Fernandes, C.M. Pereira, F. Silva, Electrochemical sensors and biosensors for determination of catecholamine neurotransmitters: a review, Talanta 160 (2016) 653–679, https://doi.org/10.1016/j.talanta.2016.06.066.

[48] Z. Xu, et al., Non-enzymatic electrochemical detection of uric acid with electrodeposited Nafion film, J. Electroanal. Chem. 841 (2019) 129–134, https://doi.org/10.1016/j.jelechem.2019.04.028.

[49] B. Yan, et al., Glassy carbon electrode modified with G-MoS2-Nafion acts as an electrochemical biosensor to determine uric acid in human serum, Mol. Med. Rep. (2018), https://doi.org/10.3892/mmr.2018.9314.

[50] Y.-K. Chih, M.-C. Yang, An 2,2′-azino-bis(3-ethylbenzthiazoline-6-sulfonic acid)-immobilized electrode for the simultaneous detection of dopamine and uric acid in the presence of ascorbic acid, Bioelectrochemistry 91 (2013) 44–51, https://doi.org/10.1016/j.bioelechem.2013.01.001.

[51] K. Berend, L.H. van Hulsteijn, R.O.B. Gans, Chloride: the queen of electrolytes? Eur. J. Intern. Med. 23 (3) (2012) 203–211, https://doi.org/10.1016/j.ejim.2011.11.013.

[52] G. Voskerician, et al., Biocompatibility and biofouling of MEMS drug delivery devices, Biomaterials 24 (11) (2003) 1959–1967, https://doi.org/10.1016/s0142-9612(02)00565-3.

[53] G. Kotzar, et al., Evaluation of MEMS materials of construction for implantable medical devices, Biomaterials 23 (13) (2002) 2737–2750, https://doi.org/10.1016/s0142-9612(02)00007-8.

[54] S.S. Stensaas, L.J. Stensaas, Histopathological evaluation of materials implanted in the cerebral cortex, Acta Neuropathol. 41 (2) (1978) 145–155, https://doi.org/10.1007/bf00689766.

[55] Y.J. Lee, H.-J. Kim, J.Y. Kang, S.H. Do, S.H. Lee, Biofunctionalization of nerve interface via biocompatible polymer-roughened Pt black on cuff electrode for chronic recording, Adv. Healthc. Mater. 6 (6) (2017) 1–12, https://doi.org/10.1002/adhm.201601022.

[56] G. Kim, H. Kim, I.J. Kim, J.R. Kim, J.I. Lee, M. Ree, Bacterial adhesion, cell adhesion and biocompatibility of Nafion films, J. Biomater. Sci. Polym. Ed. 20 (12) (2012) 1687–1707, https://doi.org/10.1163/156856208x386273.

[57] R.F.B. Turner, D.J. Harrison, R.V. Rojotte, Preliminary in vivo biocompatibility studies on perfluorosulphonic acid polymer membranes for biosensor applications, Biomaterials 12 (4) (1991) 361–368, https://doi.org/10.1016/0142-9612(91)90003-s.

[58] M.E. Gray, et al., Biocompatibility of common implantable sensor materials in a tumor xenograft model, J. Biomed. Mater. Res. B Appl. Biomater. 107 (5) (2018) 1620–1633, https://doi.org/10.1002/jbm.b.34254.

[59] A.J.T. Teo, A. Mishra, I. Park, Y.-J. Kim, W.-T. Park, Y.-J. Yoon, Polymeric biomaterials for medical implants and devices, ACS Biomater. Sci. Eng. 2 (4) (2016) 454–472, https://doi.org/10.1021/acsbiomaterials.5b00429.

[60] M.E. Gray, et al., Ovine pulmonary adenocarcinoma: a unique model to improve lung cancer research, Front. Oncol. 9 (2019) 335, https://doi.org/10.3389/fonc.2019.00335.

[61] S.J. Falk, R. Ward, N.M. Bleehen, The influence of carbogen breathing on tumour tissue oxygenation in man evaluated by computerised pO_2 histography, Br. J. Cancer 66 (5) (1992) 919–924, https://doi.org/10.1038/bjc.1992.386.
[62] S. Schreml, R.M. Szeimies, L. Prantl, S. Karrer, M. Landthaler, P. Babilas, Oxygen in acute and chronic wound healing, Br. J. Dermatol. 163 (2) (2010) 257–268, https://doi.org/10.1111/j.1365-2133.2010.09804.x.
[63] J.P.R. Moore, A. Dyson, M. Singer, J. Fraser, Microcirculatory dysfunction and resuscitation: why, when, and how, Br. J. Anaesth. 115 (3) (2015) 366–375, https://doi.org/10.1093/bja/aev163.
[64] E. Maloney-Wilensky, et al., Brain tissue oxygen and outcome after severe traumatic brain injury: a systematic review, Crit. Care Med. 37 (6) (2009) 2057–2063, https://doi.org/10.1097/CCM.0b013e3181a009f8.
[65] M.E. Gray, et al., In vivo validation of a miniaturised electrochemical oxygen sensor for measuring intestinal oxygen tension, Am. J. Physiol. Gastrointest. Liver Physiol. 317 (2019) 242–252, https://doi.org/10.1152/ajpgi.00050.2019.